scientific reports

Check for updates

OPEN

Comparing the clinical applicability of wavefront phase imaging in keratoconus versus normal eyes

Carolina Belda-Para[1,2]✉, Gonzalo Velarde-Rodríguez[3], Miriam Velasco-Ocaña[1], Juan M. Trujillo-Sevilla[1], Iván Rodríguez-Méndez[1,2], Javier Rodríguez-Martin[4], Nicolas Alejandre-Alba[3], Silvia Rodríguez-García[2] & José M. Rodríguez-Ramos[1,2]

The aim of this work is to quantitatively assess the wavefront phase of keratoconic eyes measured by the ocular aberrometer t·eyede (based on WaveFront Phase Imaging Sensor), characterized by a lateral resolution of 8.6 µm without requiring any optical element to sample the wavefront information. We evaluated the parameters: root mean square error, Peak-to-Valley, and amplitude of the predominant frequency (Fourier Transform analysis) of a section of the High-Pass filter map in keratoconic and healthy cohorts. Furthermore, we have analyzed keratoconic eyes that presented dark–light bands in this map to assess their period and orientation with the Fourier Transform. There are significant statistical differences (*p* value < 0.001) between healthy and keratoconic eyes in the three parameters, demonstrating a tendency to increase with the severity of the disease. Otherwise, the quantification of the bands reveals that the width is independent of eye laterality and keratoconic stage as orientation, which tends to be oblique. In conclusion, the quantitative results obtained with t·eyede could help to diagnose and monitor the progression of keratoconus.

Keratoconus is a progressive and noninflammatory asymmetric corneal disorder characterized by central corneal thinning and conical corneal shape. Its prevalence is about 0.138% in the whole population[1] and leads to irregular astigmatism, increased higher-order aberrations, and progressive vision loss[2–4].

In general, Keratoconus is usually graded according to the standardized Amsler–Krumeich classification[5], which includes the parameters of keratometry and the thinnest point of the cornea, as the findings observed in the biomicroscopy exploration (corneal scarring, Vogt striae, predominant corneal nerves, etc.). Recently, some authors have brought the Zernike coefficients into relevance to objectivate this classification, concretely using the vertical coma coefficient due to the large amount of this polynomial induced by the formation of the conic protrusion[6,7]. There are different techniques to obtain these values: by topographers (Placido's disk, Scheimpflug camera, etc.) or by wavefront sensors (Hartmann-Shack, WaveFront Phase Imaging, laser ray tracing, etc.). Then, it is necessary to clarify that topographers extract Zernike polynomials using the elevation map of the corneal surface, where a customized algorithm is required to apply to calculate them for each surface that depends on the manufacturer device[4], obtaining a lack of repeatability for a highly deformed cornea (like the keratoconic cornea), as has been reported in the literature[8,9]. Meanwhile, wavefront sensors acquire the phase directly by refraction of light passing through all refractive ocular surfaces. Hence, the results obtained by both methods must not have been numerically comparable without using a data treatment[10,11]. Although both acquisition methods are disparate and the plane measurement reference is different too (topographers use the cornea as the measuring plane while ocular aberrometers use the pupil plane), their comparisons could be made concerning their trends.

However, the evaluation of the keratoconic eyes by commercial ocular aberrometers (especially those that use the Hartmann-Shack sensor) is limited for different reasons. One of these is that these devices only extract up to the 8th or 10th order of Zernike polynomials because further orders have not been considered clinically necessary due to the low values obtained[12–14] but are relevant to assess pathological eyes[15]; another reason is the limited resolution of this sensor, which depends on its array of microlenses and its correspondent spots[14,16,17]. Furthermore, in moderate-severe cases, the conical surface deflects considerably the light, displaying the spots far from their reference on the image detector such as a charge-coupled device (CCD) sensor, translated as phase distortion[17,18].

[1]Wooptix S.L., Avenida Trinidad, 61 Planta 7, 38000 La Laguna, Tenerife, Canary Islands, Spain. [2]University of La Laguna, Calle Padre Herrera s/n, 38200 La Laguna, Tenerife, Canary Islands, Spain. [3]Ophthalmology Department, Fundación Jiménez Díaz University Hospital, Avenida. Reyes Católicos 2, 28040 Madrid, Spain. [4]Clinica Nivaria, Avda. Reyes Católicos, 25, Tenerife, Canary Islands, Spain. ✉email: carolina@wooptix.com

To overcome this, the WaveFront Phase Imaging (WFPI) sensor has recently been presented in the literature to measure the phase in transparent objects with more resolution than Hartmann–Shack[19], being previously validated in other technical fields such as silicon metrology[20,21], optical glass quality assessment[22,23], and tested in ophthalmology with healthy subjects and keratoconic patients by t·eyede prototype[19,24–26]. In the last work, the authors have demonstrated that this device is capable of reliably distinguishing between healthy and keratoconic eyes by means of the ocular aberrations (Astigmatism, Coma, and High Order Aberrations), besides exposing the relevance of the further orders than 10th by revealing a pattern of folds or bands in advanced keratoconus that have not been seen in phase results previously. Therefore, the analysis of the known parameters combined with the quantitative assessment of these patterns could be helpful in the diagnosis, monitoring, or treatment of keratoconus.

Previously, the map that reveals these folds had only been submitted qualitatively but can be described quantitatively using the map itself and assessing it by means of the Fourier transform (FT). This mathematical method has been applied to numerically evaluate several biological tissues featured by bands (as collagen structures) observed in other techniques[27,28]. Hence, due to the versatility of this imaging treatment, it should be applied to achieve the differences between healthy and keratoconic eyes and characterize the patterns obtained in those.

The aim of this study is to quantitatively assess the signs observed on the phase maps in keratoconus eyes against the healthy ones as well as numerically characterize the features observed in those keratoconic maps applying the Fourier Transform.

Materials and methods

Set-up: t·eyede aberrometer

The device presented in this document is the t·eyede aberrometer, whose methodology and more technical details have been described thoroughly in previous works[19,25,26]. This aberrometer can obtain the ocular phase using the WaveFront Phase Imaging sensor (Wooptix S.L., La Laguna, Tenerife, Spain), whose main advantage over other phase sensors is its lateral resolution of 8.6 µm, achieving more than 1 million measurement points for a pupil diameter of 9 mm. That fact is due to the possibility of using the pixels of a CCD sensor as measurement points without needing any other optical element to sample the ocular phase (like an array of microlenses or a pyramidal prism). The sensor captures two intensity images with 13 mm of distance among each other to recover the wavefront phase from a transparent sample[19,21].

Regarding the apparatus, it uses a Superluminescent Diode (SLD) with a wavelength of 780 nm with a bandwidth of 20 nm. The exposure time in the pupil plane is 30 ms at a power of 0.78 mW, which is under the security value of the ANSI rules (2.4 mW for this exposure time and wavelength). A Badal system corrects the patient's defocus in the range of − 10.00 D to + 10.00 D. Moreover, the device is optically optimized to avoid spurious light reaching the CCD sensor, as shown in detail in the original Fig. 1a of the Bonaque's work[19].

In addition, the set-up uses a Red Maltese Cross as the fixation target and a chinrest where the patient must be placed. Then, the position of the patient's pupil is controlled by another camera, allowing the operator to adjust the apparatus until it is centered and focused.

Patients and measurement protocol

The sample used in this paper has been described in our previous study[25]. The measurements were performed at the Hospital Universitario Fundación Jiménez Díaz (Madrid, Spain), obtaining a control cohort group composed of eyes with no ocular diseases and a pathological group with eyes diagnosed and graded as keratoconus without treatment by three experienced ophthalmologists. The Hospital Institutional Review Board approved the study protocol that met the tenets of the Declaration of Helsinki. Before t·eyede measurements, informed consent was obtained from the subjects after the nature of the study explanation. The exclusion criteria were presenting other

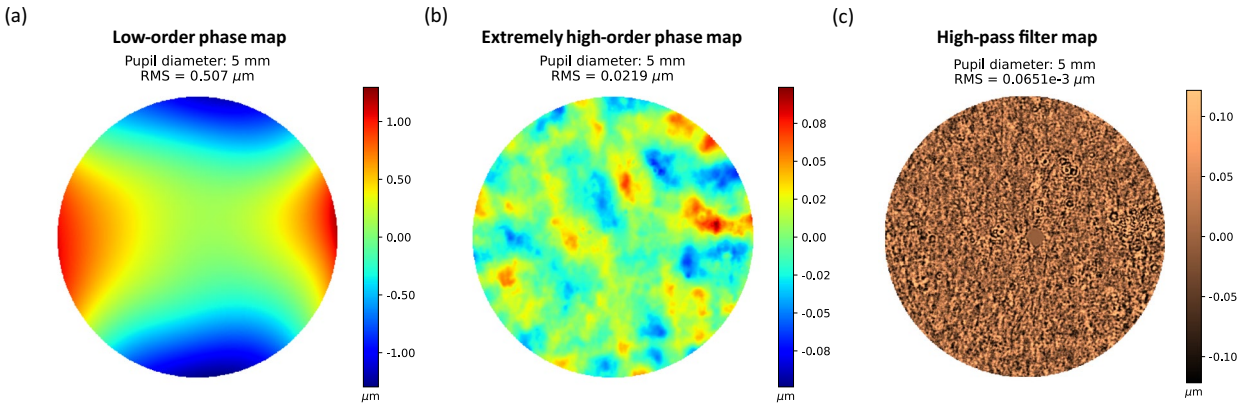

Figure 1. Healthy eye: (**a**) Low-order phase map composed of the first 65 Zernike's polynomials removing piston, tip/tilt, and defocus. (**b**) Extremely high-order map obtained from the subtraction of the rough phase and the first 65 Zernike's polynomials. (**c**) High-pass filter map of the extremely high order map (**b**).

ocular pathologies, being under the legal age, currently pregnant or breastfeeding, or participating in another interventional study within 30 days before starting this study.

Hence, the total sample is divided into two main groups: the control group presents 43 healthy eyes of 25 patients, and the study group has 43 keratoconic eyes of 27 patients. The demographic characteristics of these are summarised in Table 1.

The division of the keratoconus group between stages has been carried out based on the Pentacam Topographic Keratoconus Classification (TKC), which was corroborated by the criteria of the physicians (the decisive criteria). Only one eye classified as Healthy by the TKC was diagnosed as keratoconus concerning the ophthalmologist criteria (so it was included in the KC group), 5 eyes were classified as 'Suspect' but clinicians confirmed keratoconus diagnosis, 12 eyes were labeled as stage I, 21 eyes as stage II, 2 eyes as stage III, and 2 eyes as stage IV.

Regarding the measurement protocol with this aberrometer, the patients had their routine ophthalmological consultation previous t·eyede measurements. Then, clinicians explained the study to those patients with keratoconus diagnosis and those without ocular conditions and were voluntarily invited to sign the informed consent form that allowed the t·eyede operator to take the intensity images. After the image acquisition, the patients were invited to leave the hospital with their ophthalmological consultation concluded.

Image processing

Once the images are acquired, the WFPI software provides the high-resolution rough ocular phase map of the whole patient's natural pupil. With this information, a first phase map is displayed up to the 10th Zernike order without the coefficients of piston, tip/tilt, and defocus (this map is named as low-order map), as seen in Fig. 1a. At the same time, another processed map represents the phase resulting from the subtraction of the rough phase and the low-order phase (named as extremely high-order map), as shown in Fig. 1b.

Subsequently, the software applies a Gaussian high-pass filter to the extremely high-order map to enhance the high frequencies of the phase (named as high-pass filter map), allowing the uncovering of details hidden in the low-order map as seen in Fig. 1c, obtaining this kind of map in the ocular wavefront analysis thanks to the high resolution of the sensor[19]. This high-pass filter is applied in the frequency domain using a mask to remove frequencies lower than the cut-off value of 25 μm (considered as the fittest proved value that sharply enhanced the details observed in this map).

Quantitative evaluation of high-pass filter mapping

Since the WFPI technique has already been demonstrated to work reliably using the low-order phase to differentiate between healthy and keratoconic eyes[25], this study will quantitatively characterize the high-pass filter map to show their impact on the decision to diagnose keratoconus as well as its stage. To achieve this purpose, we first take a section of this map of 160×160 px for all the eyes and calculate its root mean square error (RMS) and peak-to-valley (PV) distance values. In the keratoconic eyes, this section was applied in a zone with neat banding, while in healthy eyes it was placed in the most uniform area possible (trying to always select the same zone in these cases) because there was no specific pattern.

Then, we obtain the FT of this section to analyze its frequency spectrum. This mathematical tool aims to convert image contents from the 'spatial' domain into 'frequency' by decomposing this information into a superposition of harmonic functions along the horizontal and vertical axes. For example, if the input image contains a periodic pattern that can be described by a single harmonic, the FT would represent an output image with a specific value of intensity (corresponding to that harmonic) in a gridding scale where its location indicates its frequency value along the x and y axes. Hence, lower frequencies are closer to the origin of the grid (associated with the thickest patterns in the spatial domain), while higher frequencies (associated with the thinnest patterns in the spatial domain) are further away[29–31]. In this analysis, the first step is to extract the amplitude of the predominant frequency in both healthy and keratoconic eyes, as well as for the different disease stages.

The next step is quantitatively assessing the banding patterns detected by attaining its spatial period and orientation using the FT, as can be seen in Fig. 2. The period (p) of the spatial light–dark bands (from the beginning of the light band to the end of the dark band) is obtained knowing the coordinates of the predominant frequency (f_X, f_Y) and calculated by the Eq. (1)[31]; meanwhile the orientation of these bands (θ) is calculated as perpendicular to the predominant frequency direction on the Fourier Transform (φ) achieved by the expression (2)[31]. In addition, all left eyes have been mirror-symmetry reflected concerning the vertical axis in the spatial domain to compare them against the right eyes using the same nasal-temporal laterality criteria independently of whether only one eye or both were measured for the same patient.

Eyes (n)	Control (43)	Keratoconus (43)
Gender (M:F ratio)	10:15	16:11
Age (years) (Mean ± SD) [Range]	40.16 ± 9.84 [27–58]	38.42 ± 11.71 [18–66]
Sph (D) (Mean ± SD) [Range]	−1.05 ± 1.90 [−6.00–2.75]	−1.28 ± 1.54 [−8.25–0.75]
Cyl (D) (Mean ± SD) [Range]	−0.70 ± 1.04 [−4.50–0.00]	−2.11 ± 1.36 [−5.00–0.00]
BCVA (Decimal) (mean ± SD) [Range]	1.06 ± 0.10 [0.9–1.2]	0.83 ± 0.20 [0.2–1]

Table 1. Demographic characteristics of control and keratoconus groups[a]. [a]*Sph* sphere value from subjective refraction, *Cyl* cylinder value from subjective refraction, *BCVA* best-corrected visual accuity.

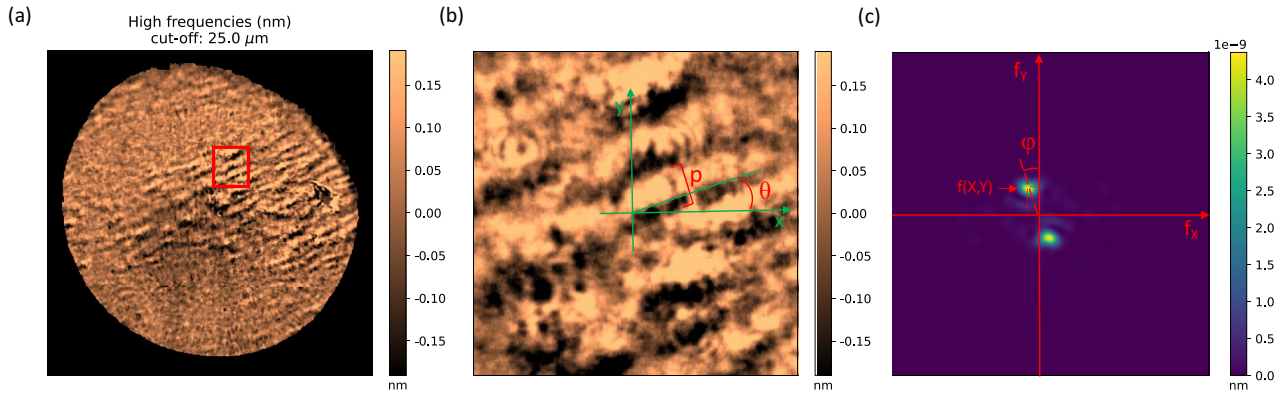

Figure 2. (**a**) High-pass filter map of a keratoconic eye with banding pattern. (**b**) The evaluated section. (**c**) The Fourier Transform of the evaluated section.

$$p = \frac{1}{\sqrt{f_X^2 + f_Y^2}} \tag{1}$$

$$\varphi = arctan\left(\frac{f_Y}{f_X}\right) \tag{2}$$

Data analysis

The programs Excel (Microsoft Office 365, v.2301) and Python (v3.9.11) have been used to process and assess the data. The mean and standard deviation values were calculated for all parameters. The statistical analysis has been applied to both main groups using the Shapiro–Wilk test to corroborate the normal distribution of the samples, and the Mann–Whitney test is used to compare both groups. The statistical significance has been established at p values < 0.05. Nevertheless, due to the low number and inequality of the sample in the severity stage groups, this step has not been carried out to compare them.

Results

High-order phase map quantitative assessment

First, we directly calculated the RMS from the high-pass filter map, whose mean value for the control group was 0.041 ± 0.007 nm (range: 0.025–0.055 nm) and 0.060 ± 0.018 nm (range: 0.036–0.117 nm) for the keratoconic group. Likewise, the PV mean value obtained for the control group was 0.20 ± 0.03 nm (range: 0.12–0.27 nm), and for the keratoconic group was 0.29 ± 0.09 nm (range: 0.18–0.59 nm). The Shapiro-Wilks test for both parameters in both groups revealed that the control sample had a normal distribution ($p > 0.1$) while the keratoconic one did not ($p < 0.001$). Therefore, the nonparametric Mann–Whitney U test was performed to compare both groups, obtaining statistically significant differences ($p < 0.001$) on both RMS and PV.

Although this analysis cannot be applied to the disease stages, the trend for each parameter concerning the grades is depicted in Figs. 3 and 4, respectively. As can be seen, RMS tends to increase with the severity stage, as PV does.

Regarding the amplitude of the predominant frequency obtained with the FT, it reached the value of $4.39e{-}12 \pm 3.66e{-}12$ nm (range: 6.12e−13–2.01e−11 nm) for the control group and $5.97e{-}11 \pm 8.91e{-}11$ nm (range: 1.77e−12–5.22e−10 nm) for the keratoconic group. Performing the same statistical analysis, in this case, the samples did not have the normal distribution according to the Shapiro–Wilks test ($p < 0.001$). Therefore, the Mann–Whitney test was carried out to compare both groups, obtaining statistically significant differences between them ($p < 0.001$). At the same time, the graphical comparison has been made between stages to conclude that the amplitude value increases according to the severity of the disease, as shown in Fig. 5.

Quantification and analysis of the banding pattern

From a total of 43 eyes with keratoconus, 33 of them had banding pattern (2 suspects of keratoconus, 8 with stage I, 19 with stage II, 2 with stage III, and 2 with stage IV), and only 2 from the 43 healthy eyes. Thus, almost 35 eyes presented a banding pattern, divided into 18 right and 17 left eyes.

Regarding the periodicity of the banding pattern, the mean obtained for the total eyes (35) was 51.4 ± 9.4 μm (range: 30.5–71.9 μm); for the right eyes (18) was 51.5 ± 11.5 μm (range: 30.5–71.9 μm); and for left eyes (17) was 51.4 ± 6.6 μm (range: 43.4–63.4 μm). If the sample is subdivided into severity stages, the healthy eyes (2) presented a mean value of 55.5 ± 13.9 μm (range: 45.7–65.4 μm), the suspect eyes had a mean value of 66.40 ± 7.91 μm (range: 60.8–71.9 μm), the mean for the stage I eyes (8) was 49.4 ± 6.8 μm (range: 38.5–58.4 μm), for the stage II

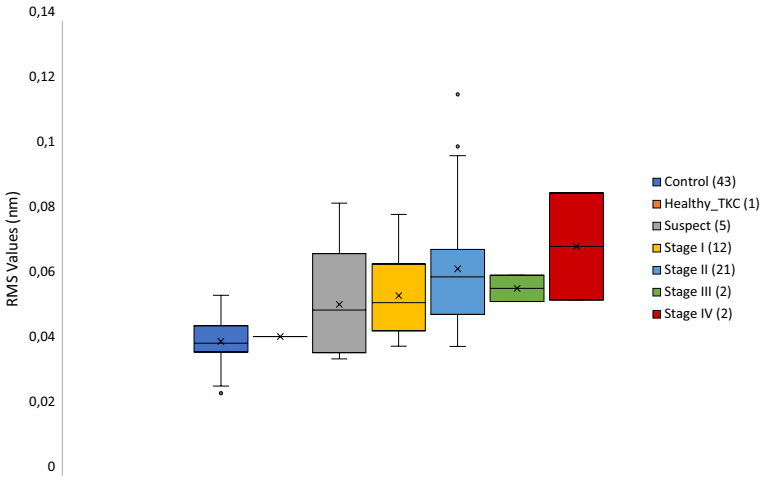

Figure 3. The root mean square error (RMS) results for each stage.

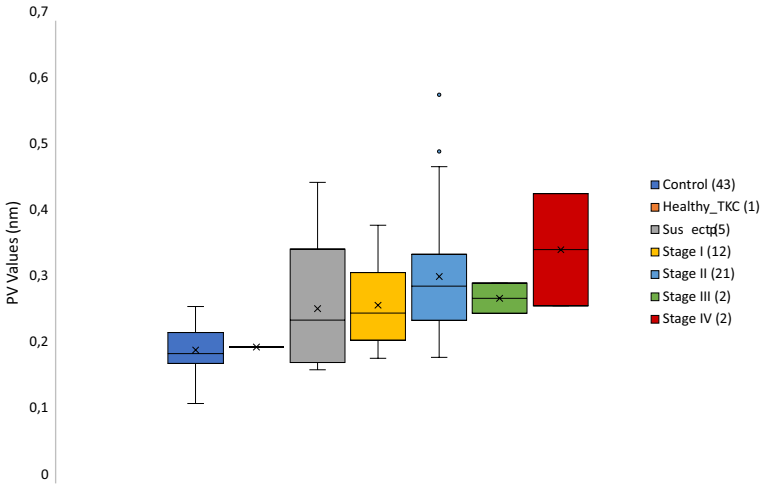

Figure 4. The peak-to-valley (PV) results for each stage.

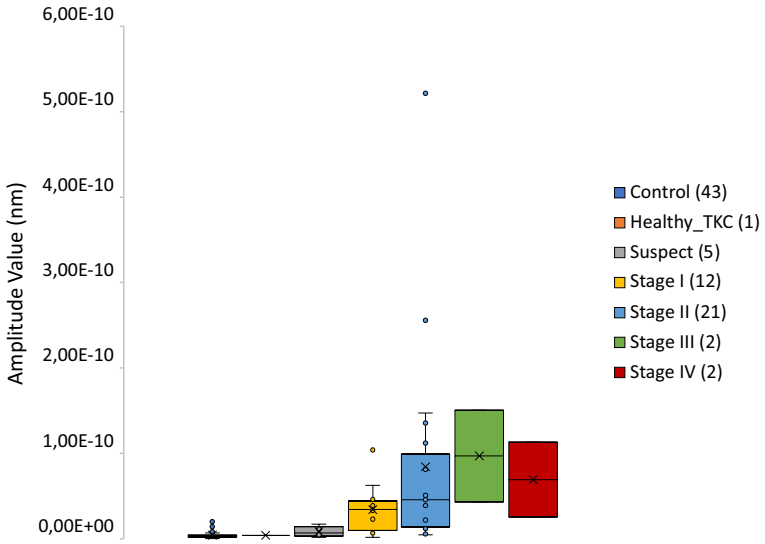

Figure 5. Representation of the amplitude tendency between stages.

(19) it was 51.4 ± 8.1 µm (range: 38.1–65.1 µm), for the stage III (2) the mean result was 55.7 ± 15.5 µm (range: 44.7–66.7 µm), and for the stage IV (2) was 37.6 ± 10.1 µm (range: 30.5–44.7 µm).

On the other hand, the orientation results were evaluated in the range of 0 (Nasal side) to 180° (Temporal side), as can be seen in Fig. 6. Comparing the total sample between the right and left eyes (Fig. 6a), the values for the right eyes (red spots) were concentrated in the oblique angles around 20° and 135°; otherwise, the values for the left eyes (blue squares) were scattered around 20° and throughout the rest of the range.

Analyzing these results by stages (Fig. 6b), for the two healthy eyes (black stars) the values were 101° and 132°, while the suspect cases (grey triangles) presented the fringes at 144° and 16°; four eyes in stage I (green spots) were obliquely positioned at approximately 20°, while the other four were dispersed throughout the rest of the angles; in stage II (yellow diamonds), nine eyes were embedded along the first 40° degrees, two orientated more obliquely at 70° approximately, and the rest of values were accounted between 115° and 150°; in stage III (purple pentagons) the two values were 119° and 25°; and at least the two eyes of stage IV (sky blue squares) had the values of 35° and 2°.

From these results, we can summarize that the period of the pattern is independent of the laterality of the eye and the stage because the values are embedded in the range of 40–60 µm, as well as the orientation is commonly oblique regardless of the eye or severity.

Discussion

In this study, we evaluated quantitatively the high-pass filter map obtained with t·eyede in a sample of both healthy and KC eyes. This specific map has been presented for the first time in the work of Bonaque-González et al.[19] in a small sample with healthy eyes where each eye has different "ocular structures" (referring to the details revealed) but without any specific pattern. However, in the subsequent study, using the initial prototype of this device to compare the aberrometry between KC and healthy eyes, we qualitatively found a characteristic

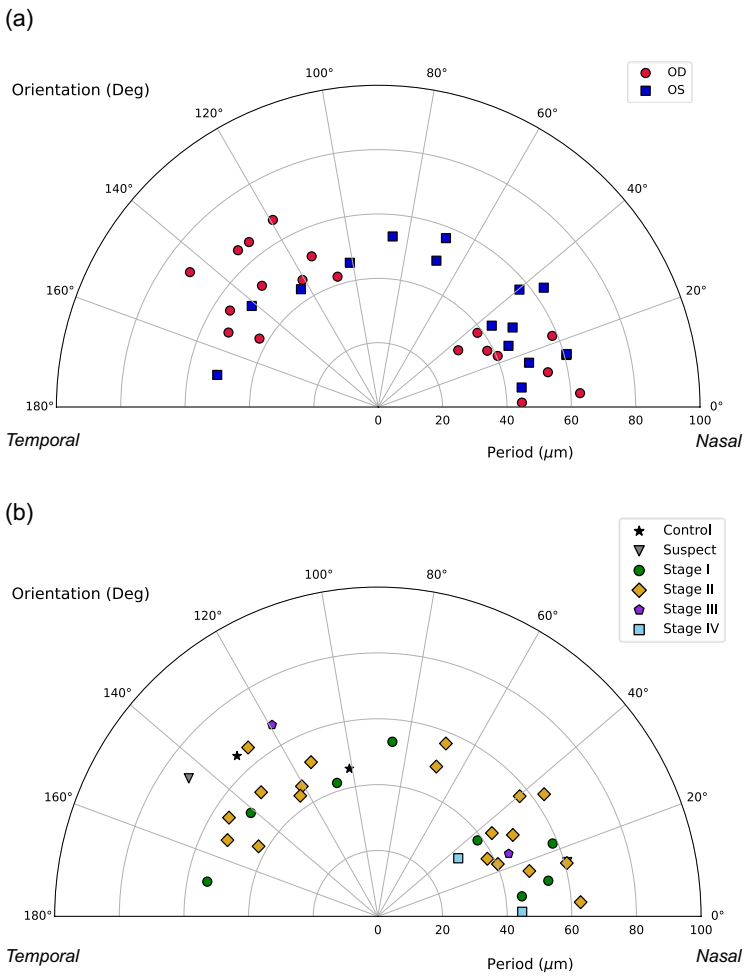

Figure 6. Orientation and period values of the banding pattern for all the eyes. (**a**) Comparison between right eyes (OD) (red spots) and left eyes (OS) (blue squares). (**b**) Comparison between stages: Control (black stars), Suspect (grey triangles), Stage I (green spots), Stage II (yellow diamonds), Stage III (purple pentagons), Stage IV (sky blue squares).

pattern in most of the maps corresponding to keratoconic eyes such as dark–light alternating bands, specifically in 76.74% of this sample, meanwhile in the rest might not be detectable due to the early stage of the disease or the great decentration of the cone concerning the pupil center[25]. These bands are noticeable due to the effect that they cause on the ocular phase, and they have never been seen before using wavefront measuring techniques because no other sensor had sufficient resolution to uncover them.

Although this event has not been observed in phase studies, several papers on keratoconic corneas inform about it using other devices such as slit-lamp microscopy[32], light microscopy[33], confocal microscopy[33–36] and second harmonic generation[37–41]. There is no unique name for this pattern because some authors refer to it as Vogt's striae[33,34], folds[36], or banding pattern[42–44]. But all of them describe it as a phenomenon produced by the stress suffered over the stromal collagen lamellae due to the outgrowth of the cone, and this event appears in almost 50% of their samples, which agrees with our percentage. One of the limitations of this study is the fact that t·eyede measures the total ocular phase and not from a single structure as the cornea, so we cannot conclude with certainty that the pattern obtained in the high-pass filter map corresponds to folds created in the stroma by corneal stress and is an isolated phenomenon of the Keratoconus disease. Then, it would be interesting for future works measuring post-surgery corneal ectasia, Pellucid Marginal Degeneration, or crosslinked-treated corneas (pre- and post-treatment). To solve this disadvantage, a prototype capable of measuring the phase of different ocular structures (tear, cornea, crystalline lens, etc.) is currently being developed in the way to know where these bands came from.

Moreover, we decided to quantitatively assess the bands found in the high-pass filter map with the Fourier Transform because it fits adequately in the study of periodic patterns like this, and many studies applied it to analyze collagen structures from different tissues[27–30]. Nevertheless, there is no unique method to assess this kind of pattern[37,39,41], and one of our following goals will be to compare Fourier methods with others, such as the Radon Transform, which is also capable of automatically detecting and quantifying the band patterns[45]. We also plan to make use of Artificial Intelligence to label automatically and individually each of the bands for better quantification of the problem and subsequent classification between those subjects who presented this pattern and those who did not, as previous authors had worked with this tool with topography and tomography descriptors to diagnose and evaluate the studied disease[46–50].

In the present work, the period of the bands obtained in the FT has a mean of 50 μm with a 95% Confidence Interval of 46–54 μm, which is associated with the width of the bands. If we go back to the previous references, these bands have been qualitatively assessed[34–37], and only Morishige et al. quantify them using confocal microscopy examination of four keratoconic eyes, revealing values along the thickness of the stroma closer to our period values[41]. Many authors discussed that the collagen lamellae of the posterior stroma run straight and parallel in vertical orientation and have the appearance of 'boarding sheets' embedded in the range of 100–200 μm, but the lamellae of the anterior stroma have thinner width and their orientation can be found as horizontally as vertically[34,51]. Hence, in the hypothetical case that our detected bands would be collagen lamellae, we cannot assure which section of the stroma is affected, but we are aware that it induces changes in the ocular wavefront phase. Mazzotta et al. concluded that the detection of such patterns, with or without Vogt's striae, could represent a relative contraindication to perform a riboflavin-UVA-induced corneal cross-linking due to the appearance of stromal haze that could lead to stromal scarring[44]. Although this assumption should be corroborated, and we do not know the severity of their sample and how this pattern is affected, we thought that t·eyede is capable of detecting accurately the early apparition of these bands and could be helpful to apply the fittest treatment according to that sign and other critical parameters.

On the other hand, in our study, the mean orientation was oblique rather than vertical, as part of the literature described[33–36,43]. Hollingsworth and Efron attached a diagram (Ref.[24], Fig. 9) of possible orientations of the stress patterns of a keratoconic left eye that are not just vertical (applicable mirror symmetrically for the right eye), and this simulation agrees with the orientations that we saw. Moreover, in the works of Tan et al. and Meek et al., the researchers observed that the alterations of the stromal collagen induce formations of "collagen bundles" centripetally disposed around the cone apex, allowing the assessment of the corneal biomechanical response in the weakest zone (the cone apex)[52,53]. In addition, Mazzotta et al.[44] showed in their observations with confocal microscopy similar patterns with vertical, horizontal, reticular, and oblique orientation also in patients without clinical evidence of Vogt's striae (as most of our subjects), reporting that these bands appear in the anterior, intermediate, and posterior stroma and would be associated with advanced progressive keratoconus, which coincides with our cases with clear evidence of this sign. Furthermore, as we presented in the previous paper, some patterns tend to bend even parallel to each other unless they run straight like Vogt's striae (Ref.[20] Fig. 3e–f), as the images that are shown in the studies with an ex vivo examination using Second Harmonic Generation[37,38] or confocal microscopy[40].

Regarding the quantitative analysis of the high-pass filter map, we calculated the RMS and PV of a section to reach other parameters that can help in the KC detection, obtaining for both metrics results statistically different between the control and the keratoconic group as we presented in the previous study with the RMS of astigmatism, coma, and high-order aberrations (HOA)[25]. For further investigations, we will consider the sample size because the sample presented was small and unequal between disease stages, so we cannot compare the marked suspect cases with the controls nor compare severe stages (III and IV) with the mid-stages (I and II) where we have more sample. Nevertheless, in our case, we saw that the values of RMS and PV tend to ascend according to the severity of the disease. For that reason, we will consider this for further studies, as we think that these parameters, combined with the others obtained by t·eyede measurement and processing (as the amplitude of the predominant frequency in FT analysis, astigmatism, and coma), may be sufficiently accurate to distinguish between normal or pathologic eye, as also between stages even if no banding is presented.

Therefore, banding patterns have been possibly observed with the current phase measurement method when they are not visible at first glance with the slit-lamp, where doctors only referenced 5 keratoconic eyes with

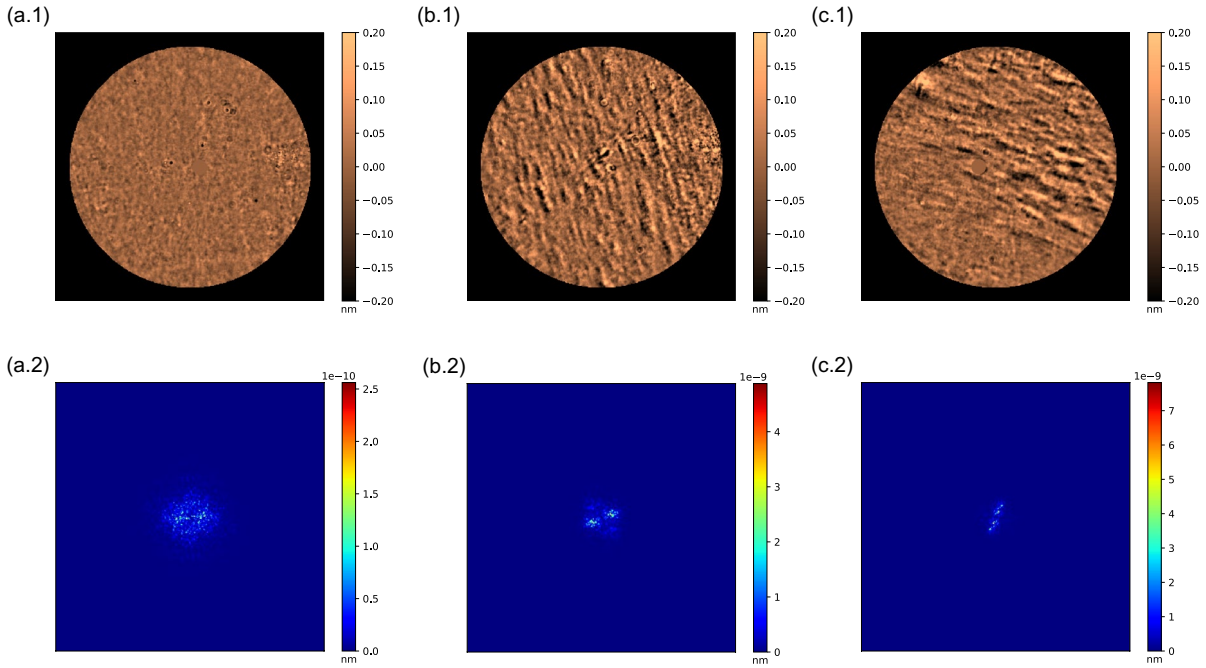

Figure 7. Examples of (**a**) a right healthy eye, (**b**) a right Stage I keratoconic eye, and (**c**) a left Stage II keratoconic eye represented by their High-Pass filter map using a pupil diameter of 5 mm (1) with their corresponding Fourier Transform representation (2).

"streaks" from those 43 evaluated. Along with this, these bands can be objectively quantified using the Fourier Transform as a reliable tool, which automatically performs the analysis without relying on any human criteria, and the distribution of the energy is appreciated clearly in its representation between healthy and keratoconic eyes, as we try to visually explain in Fig. 7. Here is presented the high-pass filter map of a healthy (Fig. 7a.1) against two keratoconic eyes with different stages (Stage I in Fig. 7b.1 and Stage II in Fig. 7c.1) with their respectively Fourier Transform representation (Fig. 7a.2, b.2, c.2). In these images it is possible to see that the energy on the healthy eye scatters along a circumference without any tendency, and the scale bar of the frequency's amplitude displays values much lower than the other two scales. Whereas, in the distributions of the keratoconic eyes, the energy is concentrated in two symmetrical lobes, which represent the predominance of the bands (perpendicular to the orientation of the lobes) regarding the rest of the details contained on the map, as well as the increase on the scale bar values in the most severe stage.

In summary, the literature refers to a pattern of dark–light bands that appear in the keratoconic cornea due to the stress suffered by the stromal collagen lamellae by the crescent protrusion of the cone, which are detectable on the moderate and several cases with the slit-lamp, confocal microscopy, and second harmonic generation examination. We observed a similar pattern using a high-resolution ocular aberrometer after processing the extremely high orders of the whole phase, reaching statistical differences between healthy and pathological eyes. Then, we can characterize this pattern using the Fourier Transform, obtaining results closer to those described in the bibliography regarding width and orientation.

Conclusions

As closure, we demonstrate that the high resolution achieved by the t·eyede aberrometer can quantitatively discern between healthy and keratoconic eyes and be the one in revealing a specific banding pattern on keratoconic eyes through the phase information. These bands can be quantitatively determined using the Fourier Transform, which can accurately characterize them by their orientation and period, obtaining that most of these bands are oblique rather than vertical and their width is approximately 50 μm. Further clinical studies with this device are needed to confirm that the presence of these bands is due to the stress suffered by the stroma during the cone formation, to understand the corneal biomechanics, and to corroborate how this event may contribute to refining the diagnosis process and its monitoring, as to assess the most appropriate treatment of the keratoconic eye.

Data availability

The datasets generated during and/or analyzed during the current study are not publicly available due to private company reasons but are available from the corresponding author upon reasonable request.

Received: 7 December 2023; Accepted: 28 April 2024
Published online: 01 May 2024

References

1. Hashemi, H. *et al.* The prevalence and risk factors for keratoconus: A systematic review and meta-analysis. *Cornea* **39**, 263–270 (2020).
2. Maeda, N. *et al.* Wavefront aberrations measured with Hartmann–Shack sensor in patients with keratoconus. *Ophthalmology* **109**, 1996–2003 (2002).
3. Heidari, Z. *et al.* Early diagnosis of subclinical keratoconus by wavefront parameters using Scheimpflug, Placido and Hartmann–Shack based devices. *Int. Ophthalmol.* **40**, 1659–1671 (2020).
4. Ozalp, O. N. U. R. & Atalay, E. R. A. Y. Belin ABCD progression display identifies keratoconus progression earlier than conventional metrics. *Am. J. Ophthalmol.* **236**, 45–52 (2022).
5. Krumeich, J. H., Daniel, J. & Knülle, A. Live-epikeratophakia for keratoconus. *J. Cataract Refract. Surg.* **24**, 456–463 (1998).
6. Alió, J. L. & Shabayek, M. H. Corneal higher order aberrations: a method to grade keratoconus. *J. Refract. Surg.* **22**, 539–545 (2006).
7. Ortiz-Toquero, S., Fernandez, I. & Martin, R. Classification of keratoconus based on anterior corneal high-order aberrations: a cross-validation study. *Optom. Vis. Sci.* **97**, 169–177 (2020).
8. Pérez-Merino, P. *et al.* Ocular and optical coherence tomography-based corneal aberrometry in keratoconic eyes treated by intracorneal ring segments. *Am. J. Ophthalmol.* **157**, 116–127 (2014).
9. Piñero, D. P., Alió, J. L., Alesón, A., Escaf, M. & Miranda, M. Pentacam posterior and anterior corneal aberrations in normal and keratoconic eyes. *Clin. Exp. Optom.* **92**, 297–303 (2009).
10. Gobbe, M. & Guillon, M. Corneal wavefront aberration measurements to detect keratoconus patients. *Contact Lens Anterior Eye.* **28**, 57–66 (2005).
11. Tunç, U. *et al.* Repeatability and reliability of measurements obtained by the combined Scheimpflug and Placido-disk tomography in different stages of keratoconus. *EYE* **35**, 2213–2220 (2021).
12. Iskander, D. R., Collins, M. J. & Davis, B. Optimal modeling of corneal surfaces with Zernike polynomials. *IEEE Trans. Bio-Med. Eng.* **48**, 87–95 (2001).
13. Klyce, S. D., Karon, M. D. & Smolek, M. K. Advantages and disadvantages of the Zernike expansion for representing wave aberration of the normal and aberrated eye. *J. Refract. Surg.* **20**, S537–S541 (2004).
14. Prieto, P. M., Vargas-Martín, F., Goelz, S. & Artal, P. Analysis of the performance of the Hartmann–Shack sensor in the human eye. *J. Opt. Soc. Am.* **17**, 1388 (2000).
15. Smolek, M. K. & Klyce, S. D. Goodness-of-prediction of Zernike polynomial fitting to corneal surfaces. *J. Cataract Refract. Surg.* **31**, 2350–2355 (2005).
16. López-Miguel, A. *et al.* Precision of a commercial Hartmann-Shack aberrometer: limits of total wavefront laser vision correction. *Am. J. Ophthalmol.* **154**, 799–807 (2012).
17. Jinabhai, A. N. Customised aberration-controlling corrections for keratoconic patients using contact lenses. *Clin. Exp. Optom.* **103**, 31–43 (2020).
18. Jinabhai, A., Radhakrishnan, H. & O'Donnell, C. Repeatability of ocular aberration measurements in patients with keratoconus. *Ophthalmic Physiol. Opt.* **31**, 588–594 (2011).
19. Bonaque-González, S. *et al.* The optics of the human eye at 8.6 μm resolution. *Sci. Rep.* **11**, 1–12 (2021).
20. Trujillo-Sevilla, J., Ramos-Rodríguez, J. M. & Gaudestad, J. Roughness and nanotopography measurement of a Silicon Wafer using Wave Front Phase Imaging: High speed single image snapshot of entire wafer producing sub nm topography data. In *Proceedings of IEEE.* 1–8 (2020).
21. Trujillo-Sevilla, J. M., Casanova Gonzalez, O., Bonaque-González, S., Gaudestad, J. & Rodríguez Ramos, J. M. High-resolution wavefront phase sensor for silicon wafer metrology. In *Proceedings SPIE 10925, Photonic Instrumentation Engineering VI*. Vol. 109250I, 108–117 (2019).
22. Velasco-Ocaña, M., Bonaque-González, S., Trujillo-Sevilla, J. M. & Rodríguez-Ramos J.M. Novel wavefront phase sensor as objective glass quality inspector. In *UK Optical Design Meeting* (2019).
23. Trujillo-Sevilla, J. M., Velasco-Ocaña, M., Bonaque-González, S., Belda-Para, C. & Rodríguez-Ramos, J. M. Wavefront phase measurement of striae in optical glass. *Appl. Opt.* **61**, 3912 (2022).
24. Bonaque-González, S. *et al.* New high-resolution wavefront sensing ophthalmic technique for the characterization of ocular optics. *SPIE-Int. Soc. Opt. Eng.* **67** (2020).
25. Velarde-Rodriguez, G. *et al.* Ultra-high resolution optical aberrometry in patients with keratoconus: A cross-sectional study. *Ophthalmol. Ther.* **12**, 1569–1582 (2023).
26. Bonaque-Gonzalez, S., Rodriguez-Ramos, J. M. & Sicilia-Cabrera, M. Extremely high resolution ocular aberrometry up to 2.4 million points. *Invest. Ophthalmol. Vis. Sci.* **60**, 603 (2019).
27. Rao, R. A. R., Mehta, M. R. & Toussaint Jr., K. C. Quantitative analysis of biological tissues using Fourier transform-second-harmonic generation imaging. *Proc. SPIE.* **7569**, 337–345 (2010).
28. Palmer, B. M. & Bizios, R. Quantitative characterization of vascular endothelial cell morphology and orientation using Fourier transform analysis. *J. Biomech. Eng.* **119**, 159–165 (1997).
29. Ayres, C. *et al.* Modulation of anisotropy in electrospun tissue-engineering scaffolds: Analysis of fiber alignment by the fast Fourier transform. *Biomaterials* **27**, 5524–5534 (2006).
30. Rao, R. A. R., Mehta, M. R. & Toussaint, K. C. Fourier transform-second-harmonic generation imaging of biological tissues. *Opt. Express* **17**, 14534–14542 (2009).
31. Goodman, J. W. *Introduction to Fourier Optics* (Roberts and Company Publishers, 2005).
32. Szczotka, L. B., Barr, J. T. & Zadnik, K. A summary of the findings from the Collaborative Longitudinal Evaluation of Keratoconus (CLEK) Study. *Optometry* **72**, 574–584 (2001).
33. Hollingsworth, J. G., Bonshek, R. E. & Efron, N. Correlation of the appearance of the keratoconic cornea in vivo by confocal microscopy and in vitro by light microscopy. *Cornea* **24**, 397–405 (2005).
34. Hollingsworth, J. G. & Efron, N. Observations of banding patterns (Vogt striae) in keratoconus: A confocal microscopy study. *Cornea* **24**, 162–166 (2005).
35. Mocan, M. C., Yilmaz, P. T., Irkec, M. & Orhan, M. The significance of Vogt's striae in keratoconus as evaluated by in vivo confocal microscopy. *Clin. Exp. Ophthalmol.* **36**, 329–334 (2008).
36. Uçakhan, Ö. Ö., Kanpolat, A., Yilmaz, N. & Özkan, M. In vivo confocal microscopy findings in keratoconus. *Eye Contact Lens* **32**, 183–191 (2006).
37. Tan, H. Y. *et al.* Multiphoton fluorescence and second harmonic generation imaging of the structural alterations in keratoconus ex vivo. *Invest. Ophthalmol. Vis. Sci.* **47**, 5251–5259 (2006).
38. Lo, W. *et al.* Fast Fourier transform-based analysis of second-harmonic generation image in keratoconic cornea. *Invest. Ophthalmol. Vis. Sci.* **53**, 3501–3507 (2012).
39. Mercatelli, R. *et al.* Three-dimensional mapping of the orientation of collagen corneal lamellae in healthy and keratoconic human corneas using SHG microscopy. *J. Biophotonics* **10**, 75–83 (2017).
40. Morishige, N. *et al.* Second-harmonic imaging microscopy of normal human and keratoconus cornea. *Invest. Ophthalmol. Vis. Sci.* **48**, 1087–1094 (2007).

41. Morishige, N. *et al.* Quantitative analysis of collagen lamellae in the normal and keratoconic human cornea by second harmonic generation imaging microscopy. *Invest. Ophthalmol. Vis. Sci.* **55**, 8377–8385 (2014).
42. Borderie, V. M. *et al.* Banding patterns: Exploring a new feature in corneal stroma organization. *Invest. Ophthalmol. Vis. Sci.* **58**, 3906–3906 (2017).
43. Grieve, K. *et al.* Stromal striae: A new insight into corneal physiology and mechanics. *Sci. Rep.* **7**, 13584 (2017).
44. Mazzotta, C., Balestrazzi, A., Baiocchi, S., Traversi, C. & Caporossi, A. Stromal haze after combined riboflavin-UVA corneal collagen cross-linking in keratoconus: In vivo confocal microscopic evaluation. *Clin. Exp. Ophthalmol.* **35**, 580–582 (2007).
45. Oliva-García, R. *et al.* A local real-time bar detector based on the multiscale Radon transform. *Real-Time Image Process. Deep Learn.* **12102**, 76–90 (2022).
46. Lopes, B. T. *et al.* Enhanced tomographic assessment to detect corneal ectasia based on artificial intelligence. *Am. J. Ophthalmol.* **195**, 223–232 (2018).
47. Saad, A. & Gatinel, D. Topographic and tomographic properties of forme fruste keratoconus corneas. *Invest. Ophthalmol. Vis. Sci.* **51**, 5546–5555 (2010).
48. Saad, A. & Gatinel, D. Validation of a new scoring system for the detection of early forme of keratoconus. *Int. J. Keratoconus Ectatic Corneal Dis.* **1**, 100–108 (2012).
49. Ruiz Hidalgo, I. *et al.* Evaluation of a machine-learning classifier for keratoconus detection based on Scheimpflug tomography. *Cornea* **35**, 827–832 (2016).
50. Arbelaez, M. C., Versaci, F., Vestri, G., Barboni, P. & Savini, G. Use of a support vector machine for keratoconus and subclinical keratoconus detection by topographic and tomographic data. *Ophthalmology* **119**, 2231–2238 (2012).
51. Komai, Y. & Ushikif, T. The three-dimensional organization of collagen fibrils in the human cornea and sclera. *Invest. Ophthalmol. Vis. Sci.* **32**, 2244–2258 (1991).
52. Tan, H. Y. *et al.* Characterizing the morphologic changes in collagen crosslinked-treated corneas by Fourier transform-second harmonic generation imaging. *J. Cataract Refract. Surg.* **39**, 779–788 (2013).
53. Meek, K. M. *et al.* Changes in collagen orientation and distribution in keratoconus corneas. *Invest. Ophthalmol. Vis. Sci.* **46**, 1948–1956 (2005).

Acknowledgements

We would like to thank Dr. José Gil Marichal Hernández for his advice and evaluation of the quantitative analysis.

Author contributions

C.B.P. contributed to all stages of the project, M.V.O. contributed to all stages of the project except data acquisition, J.M.T.S. contributed to the software used in the work and the manuscript review, I.R.M. contributed to the software used in the work and the manuscript review, J.M.R.R. contributed to all stages of the project except data acquisition, S.R.G. contributed to substantively review the manuscript, G.V.R. contributed to the acquisition of the data and the manuscript review, N.A.A. contributed to the acquisition of the data and the manuscript review, J.R.M. contributed to substantively review the manuscript.

Competing interests

The authors declare no competing interests.

Additional information

Correspondence and requests for materials should be addressed to C.B.-P.